electronics

MDPI

Article

Dynamical System-Based Fuzzy Adaptive Admittance Control for Uncertain Environments

Jaeyun Sim, Yonoo Kim, Eui-Chan Kim, Eunseop Song, Seungyeon Lee, Jaeyoon Sim and Hyouk Ryeol Choi *

School of Mechanical Engineering, Sungkyunkwan University (SKKU), Suwon 16419, Republic of Korea; wodbs1118@g.skku.edu (J.S.)
* Correspondence: choihyoukryeol@gmail.com

Abstract

This paper presents a fuzzy-based adaptive admittance control (FAAC) framework for position-controlled robots in uncertain contact environments. The proposed FAAC regulates admittance parameters using three fuzzy adaptation maps rather than directly generating robot control inputs. The Mass-Adaptation Fuzzy Map (MAFM) adjusts the dominant virtual mass eigenvalue, the Damper–Mass Ratio Fuzzy Map (DMRFM) adapts the damping-related ratio, and the Rendering-Quality Supervisory Fuzzy Map (RQ-SFM) restricts unsafe low-mass adaptation based on rendering quality and vibration metrics. An energy-tank-based admissibility filter is integrated to preserve passivity during online parameter adaptation and contact transitions. Comparative simulations against a stiffness-adaptive baseline and an ablated mass–damping adaptive baseline under nominal, noisy, and filtered sensing conditions verify the robustness of the proposed architecture. Experiments on a UR10 polishing task further show that the proposed FAAC improves force-tracking consistency and contact-maintenance robustness compared with fixed-parameter AAC baselines and FAAC-M. In particular, the proposed FAAC achieved the lowest force standard deviation of 2.76 N and no contact-loss events, whereas the baseline AAC controllers exhibited force fluctuations associated with abrupt desired stiffness changes during contact. These results demonstrate the effectiveness of FAAC for robust robot–environment interaction under uncertain contact conditions.

Keywords: adaptive admittance control; fuzzy logic control; energy-tank passivity; force tracking; discrete-time simulation; human–robot interaction

Academic Editors: Qi Zou, Guanyu Huang, Zhibo Sun, Chonggang Du, Shuo Zhang, Hongyan Tang, Yueyuan Zhang and Le Bao

Received: 14 April 2026
Revised: 7 May 2026
Accepted: 8 May 2026
Published: 11 May 2026

1. Introduction

Robotic contact tasks such as assembly, polishing, and grinding require precise force regulation against environments whose stiffness is often unknown or time-varying [1,2]. Since most industrial manipulators provide position-level interfaces for safety, reliability, and ease of implementation, indirect force control through admittance and impedance laws is widely used to shape robot–environment interactions [3,4]. However, fixed-parameter admittance controllers are sensitive to contact stiffness variations. They may exhibit steady-state force errors, slow convergence, excessive overshoot, or unstable transient behavior when the actual contact condition deviates from the nominal design point [5].

To address these issues, adaptive, optimization-based, learning-based, and passivity-oriented approaches have been studied. Adaptive variable impedance control improves force regulation by changing interaction parameters under dynamic contact conditions [6].

Model-predictive variable impedance control has also been investigated to achieve an adaptive tradeoff between precision and compliance [7]. More recently, learning-based and optimization-based methods have been introduced to improve admittance or impedance adaptation performance in robotic contact tasks [8–11]. In parallel, passivity-oriented variable stiffness and admittance strategies, including energy-tank-based methods, have been developed to enhance stability and compliant behavior in uncertain environments [12–15].

Despite these advances, several challenges remain. These challenges are particularly important in force-controlled surface-contact tasks, such as polishing, grinding, and assembly. In these tasks, force fluctuation, excessive overshoot, or temporary contact loss can directly degrade task quality and contact reliability.

First, many adaptive admittance methods mainly regulate stiffness-related behavior. This improves steady-state force tracking, but it does not fully address transient performance when the contact condition deviates from the nominal design case. In addition, abrupt stiffness changes during continuous contact can induce transient force drops or contact-loss events. This issue becomes more severe when the virtual mass and damping are fixed.

Second, simultaneous adaptation of virtual mass and damping can improve responsiveness and stability. However, improper parameter updates may inject energy into the closed-loop interaction. In contact force control, this injected energy can increase force overshoot and excite oscillatory behavior. It can also degrade continuous-contact reliability, particularly when the outer admittance loop is implemented through a position-controlled inner loop.

Third, in position-controlled robots, the outer admittance loop must be rendered through an inner position-control loop. Stability problems can arise when the interacting environment becomes stiff or when the admittance response becomes too aggressive [13]. If the outer-loop response becomes too aggressive, the commanded virtual admittance dynamics may not be accurately realized. This rendering degradation can lead to force oscillation, degraded tracking, or contact instability. Therefore, an effective controller should coordinate force-tracking performance, parameter adaptation, rendering quality, and passivity preservation in a unified structure.

In this work, we propose a fuzzy-based adaptive admittance control (FAAC) framework for position-controlled robots operating in uncertain contact environments. The proposed FAAC is not a standalone fuzzy controller that directly generates the robot control input. Instead, it uses fuzzy adaptation maps to regulate the parameters of a dynamical-system-based admittance controller. The admittance controller generates the command position x_c, and this command is tracked by the inner-loop robot position controller. Thus, the overall architecture consists of two control loops: an outer-loop force controller and an inner-loop position controller.

The main contributions of this paper are summarized as follows:

- We propose a fuzzy-based adaptive admittance framework that explicitly adapts the dominant-axis virtual mass $\lambda_{M,3}$ and damping-related ratio r_{MD}, while regulating stiffness-related behavior for force tracking. The mass adaptation improves responsiveness or suppresses aggressive transients depending on the interaction state. The damper–mass ratio adaptation adjusts the stability–adaptability tradeoff.
- We develop a simulator-guided fuzzy rule design procedure for the Mass-Adaptation Fuzzy Map (MAFM). The force-error and force-error-derivative plane is partitioned according to representative transient contact-response patterns. Each region is then translated into a bandwidth-oriented mass-adaptation rule, making the rule table interpretable rather than arbitrary.

- We introduce a Damper–Mass Ratio Fuzzy Map (DMRFM) that adapts the damping behavior through the ratio variable r_{MD} rather than directly updating the damping eigenvalue. This ratio-based parameterization makes the damping-ratio distribution more interpretable in the $(\lambda_{M,3}, r_{MD})$ domain. It also enables fuzzy regulation of the stability–adaptability tradeoff during contact.
- We introduce a Rendering-Quality Supervisory Fuzzy Map (RQ-SFM) that monitors the rendering-quality index ε and the motion-level vibration $\mathrm{STD}(x_c - x)$. This supervisory map constrains the lower bound of the virtual mass to prevent unsafe low-mass adaptation when the inner position loop cannot reliably render the desired admittance dynamics.
- We integrate an energy-tank-based admissibility filter between the fuzzy adaptation maps and the passivity-preserved admittance controller. Candidate parameter updates are applied only when they satisfy both adaptive bounds and energy-tank constraints. This prevents excessive active energy injection during online adaptation and contact transitions.
- We validate the proposed architecture through comparative simulations and polishing experiments. In simulation, the proposed full FAAC is compared with a stiffness-adaptive AAC baseline and an ablated mass–damping adaptive baseline. The robustness of the method is further examined under noisy and low-pass-filtered force feedback. In experiments, the proposed FAAC is compared with two fixed-mass–damping AAC baselines and FAAC-M on a UR10 polishing task. This experiment evaluates force-tracking consistency and contact-maintenance robustness.

The overall control structure is illustrated in Figure 1. The lower part of the figure shows the complete cascade architecture. The desired force F_d and measured external force F_{ext} are used to compute the force-control input to the outer-loop FAAC block. The FAAC block generates the admittance command position x_c, which is tracked by the robot position controller. The robot then interacts with the environment, and the resulting position x and external force F_{ext} are fed back to the outer-loop force controller.

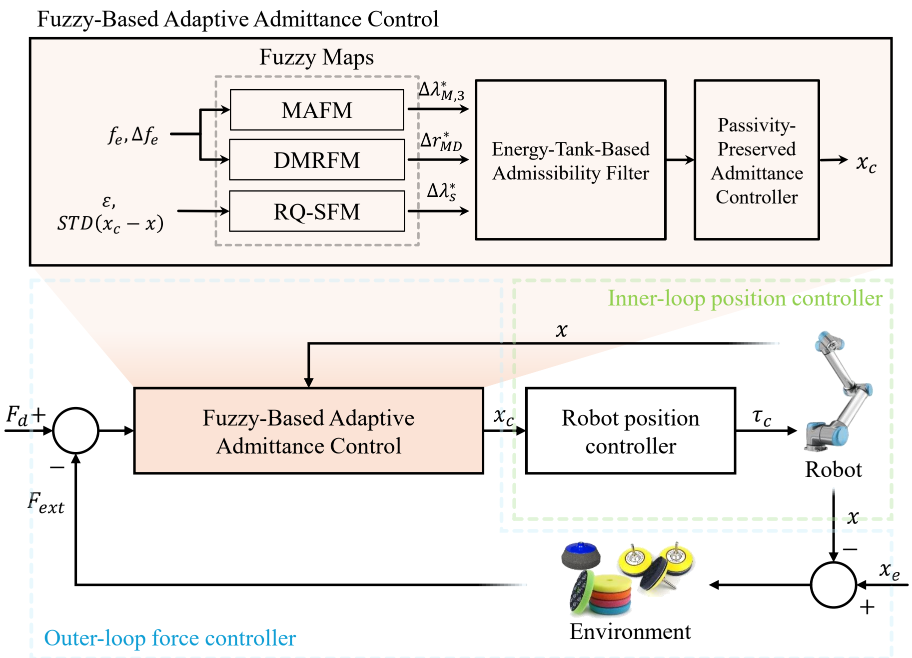

Figure 1. Overall architecture of the proposed fuzzy-based adaptive admittance control framework. The lower diagram shows the cascade structure composed of the outer-loop force controller and the inner-loop robot position controller. The upper diagram details the internal structure of the FAAC block.

The MAFM and DMRFM use f_e and Δf_e to generate candidate updates for the dominant mass eigenvalue $\Delta\lambda^*_{M,3}$ and the damper–mass ratio Δr^*_{MD}, respectively. The RQ-SFM uses the rendering-quality index ε and the position-error standard deviation $\mathrm{STD}(x_c - x)$ to generate the candidate lower-bound update $\Delta\lambda^*_s$. These candidate updates are filtered by the energy-tank-based admissibility mechanism before being applied to the passivity-preserved admittance controller.

The upper part of Figure 1 details the internal structure of the FAAC block. The MAFM and DMRFM use the force error f_e and its discrete-time derivative Δf_e to generate candidate updates $\Delta\lambda^*_{M,3}$ and Δr^*_{MD}, respectively. The RQ-SFM uses the rendering-quality index ε and the position-error standard deviation $\mathrm{STD}(x_c - x)$ to generate the candidate lower-bound update $\Delta\lambda^*_s$. These candidate updates are passed through the energy-tank-based admissibility filter before being applied to the passivity-preserved admittance controller. This structure clarifies that the fuzzy maps determine the desired direction of parameter adaptation. The energy tank then determines whether the corresponding update is energetically admissible.

2. Control Background

Dynamical-System-Based Admittance Control.

We implement admittance control on a position-controlled robot by shaping its translational response to the measured external force as a second-order dynamical system:

$$M_d\,\ddot{x}_c + D_d\big(\dot{x}_c - \dot{x}_d\big) = F_{\mathrm{ext}}, \tag{1}$$

$$\dot{x}_d = D_d^{-1}\big[K_d\,(x_r - x_c) - F_d\big], \tag{2}$$

where $x_c \in \mathbb{R}^3$ is the admittance-generated command position, $x_r \in \mathbb{R}^3$ is the reference position, $\dot{x}_d \in \mathbb{R}^3$ is the desired velocity term generated by the force-regulation law, and $F_{\mathrm{ext}}, F_d \in \mathbb{R}^3$ are the measured external force and desired contact force, respectively. The matrices M_d, D_d, and $K_d \in \mathbb{R}^{3\times 3}$ denote the virtual inertia, damping, and stiffness matrices. In this study, M_d and D_d are implemented as symmetric positive-definite matrices, whereas K_d is implemented as a symmetric positive-semi-definite matrix because the dominant-axis stiffness can be set to zero during contact force regulation. These matrices are adapted in a task-aligned eigenbasis. Since the proposed controller regulates only translational force interaction and the robot orientation is handled separately by the inner position controller, orientation dynamics are omitted.

To enable intuitive and axis-wise parameter adaptation, each admittance parameter matrix $\Sigma_d \in \{M_d, D_d, K_d\}$ is represented in the task-aligned eigenbasis as

$$\Sigma_d = Q^T \Lambda_\Sigma Q, \qquad \Lambda_\Sigma = \mathrm{diag}(\lambda_{\Sigma,1}, \lambda_{\Sigma,2}, \lambda_{\Sigma,3}), \tag{3}$$

where $\lambda_{\Sigma,i}$ is the eigenvalue associated with the principal direction Q_i. The eigenvector matrix $Q = [Q_1\ Q_2\ Q_3]$ is constructed such that Q_3 is aligned with the commanded contact-force direction. Specifically, when a nonzero desired force is commanded, the contact axis is defined as

$$Q_3 = \frac{F_d}{\|F_d\|}. \tag{4}$$

The remaining orthonormal axes are constructed using the tool-frame z-axis $V_{\mathrm{tool},z}$ as a reference:

$$
\begin{aligned}
V_b &= Q_3 \times V_{\mathrm{tool},z}, \\
Q_1 &= \frac{V_b}{\|V_b\|}, \\
Q_2 &= Q_3 \times Q_1.
\end{aligned}
\tag{5}
$$

If Q_3 is nearly parallel to $V_{\mathrm{tool},z}$, an alternative nonparallel tool-frame axis is used to avoid singularity in the cross product. If no contact force is commanded, i.e., $F_d = 0$, the task-aligned basis is not defined by the desired force; therefore, Q is set to the end-effector rotation matrix R_{EE}.

In this eigenbasis, the measured and desired forces are decomposed as

$$
\begin{aligned}
F_{\mathrm{ext}} &= Q F'_{\mathrm{ext}}, \qquad F'_{\mathrm{ext}} = [f'_{\mathrm{ext},1}, f'_{\mathrm{ext},2}, f'_{\mathrm{ext},3}]^T, \\
F_d &= Q_3 f_d, \qquad f_d \in \mathbb{R}.
\end{aligned}
\tag{6}
$$

Here, F'_{ext} denotes the external-force components expressed along the principal axes Q_i, and f_d is the scalar desired force along the contact axis Q_3. In the proposed FAAC, the dominant-axis eigenvalues $\lambda_{M,3}$, $\lambda_{D,3}$, and $\lambda_{K,3}$ are adapted online because the third axis corresponds to the contact-force regulation direction. In particular, $\lambda_{K,3}$ may be reduced to zero during contact-force regulation to remove steady-state force error, while M_d and D_d remain positive definite to preserve well-posed admittance dynamics. Equations (1)–(6) therefore define a translational admittance controller whose parameters can be adjusted in a physically interpretable and decoupled task-aligned basis.

3. Problem Statement

3.1. Limitations of Conventional Admittance Parameterization

To clarify the limitations of conventional admittance parameterization, we analyze the force-error dynamics along the dominant contact axis. In this scalar analysis, the environment is modeled as a linear spring:

$$
f_{\mathrm{ext}} = -k_e x_c, \tag{7}
$$

where k_e is the contact stiffness and x_c is the admittance-generated displacement along the contact direction. For simplicity, the reference position is set to zero, i.e., $x_r = 0$. The one-dimensional admittance law can then be written as

$$
m_d \ddot{x}_c + d_d \dot{x}_c + k_d (x_c - x_r) = f_{\mathrm{ext}} - f_d = -k_e x_c - f_d, \tag{8}
$$

which becomes

$$
m_d \ddot{x}_c + d_d \dot{x}_c + (k_d + k_e) x_c = -f_d. \tag{9}
$$

Taking the Laplace transform of Equation (9) gives

$$
\left(m_d s^2 + d_d s + k_d + k_e \right) X_c(s) = -F_d(s). \tag{10}
$$

Since $F_{\mathrm{ext}}(s) = -k_e X_c(s)$, the force-tracking transfer function is obtained as

$$
\frac{F_{\mathrm{ext}}(s)}{F_d(s)} = \frac{k_e}{m_d s^2 + d_d s + k_d + k_e}. \tag{11}
$$

For a step command $F_d(s) = A/s$, the steady-state force response is

$$f_{\text{ext,ss}} = \frac{k_e}{k_d + k_e} A. \tag{12}$$

Therefore, the steady-state force-tracking error becomes

$$\Delta f_{ss} = f_{\text{ext,ss}} - A = -\frac{A k_d}{k_d + k_e}. \tag{13}$$

This result shows that zero steady-state force error requires $k_d = 0$ under the linear contact model.

This analysis indicates that the admittance stiffness parameter strongly affects steady-state force accuracy. Updating the stiffness parameter online can therefore improve force-tracking performance compared with purely fixed-parameter admittance control. However, stiffness-only adaptation is generally insufficient to ensure both fast convergence and stable transient behavior under large variations in contact stiffness. Once k_d is reduced to improve steady-state force accuracy, the transient response is mainly governed by the virtual mass m_d and damping d_d. This limitation motivates the proposed FAAC framework, which extends conventional adaptive admittance control by jointly regulating mass and damping through fuzzy inference and supervisory constraints.

3.2. Effect of M_d and D_d on Dynamic Behavior

From Equation (9), the damping ratio ζ and natural frequency ω_n of the scalar contact-axis dynamics are given by

$$\zeta = \frac{d_d}{2\sqrt{m_d(k_d + k_e)}}, \qquad \omega_n = \sqrt{\frac{k_d + k_e}{m_d}}. \tag{14}$$

After stiffness adaptation reduces k_d toward zero, the stiffness term has a reduced effect on force-tracking accuracy. The damping ratio and natural frequency can then be approximated as

$$\zeta \approx \frac{d_d}{2\sqrt{m_d k_e}}, \qquad \omega_n \approx \sqrt{\frac{k_e}{m_d}}. \tag{15}$$

Equations (14) and (15) show that the transient response depends on the contact stiffness. Thus, the same admittance parameters can produce different dynamic behavior under different contact conditions. Therefore, fixed values of m_d and d_d cannot simultaneously guarantee fast response in low-stiffness contact and stable behavior in high-stiffness contact. This trade-off can be summarized by four representative parameter–environment scenarios under low- and high-stiffness contact conditions. These scenarios are used only to explain the effect of m_d, d_d, and k_e on the transient response.

- **Scenario 1 (low k_e, low m_d, low d_d):** The system has a relatively high response speed and can track fast force commands. This setting is beneficial for responsiveness in compliant contact.
- **Scenario 2 (low k_e, high m_d, high d_d):** The system becomes overly conservative. As a result, the force response becomes slower. The tracking responsiveness is also degraded in compliant contact.
- **Scenario 3 (high k_e, low m_d, low d_d):** The natural frequency increases, and the damping ratio may become insufficient. Therefore, the system can become sensitive to disturbances. It may also exhibit oscillatory or aggressive transient behavior.

- **Scenario 4 (high k_e, high m_d, high d_d):** The response becomes more stable because the effective bandwidth is reduced. In addition, sufficient damping is provided. This setting is beneficial for suppressing aggressive transients in stiff contact.

This analysis explains why the proposed controller adapts the mass and damping parameters in addition to the stiffness parameter. A smaller virtual mass is beneficial for responsiveness in compliant contact. In contrast, a larger virtual mass with sufficient damping is required to suppress aggressive transient behavior under stiff contact.

3.3. Importance of Rendering Quality

The proposed admittance controller is implemented as an outer force-control loop on top of the robot's inner position-control loop. In such a cascade structure, the desired virtual admittance dynamics can be accurately rendered only when the outer-loop response remains sufficiently slower than the inner position-loop response. If the outer force-control loop becomes too aggressive, the inner position controller cannot accurately realize the commanded admittance motion. This can distort the force response and cause potential instability.

To monitor this degradation, we define the rendering-quality index along the dominant contact axis as

$$\varepsilon(t) = f'_{\text{ext},3}(t) - f_d(t) - (m_d \ddot{x}_{c,3}(t) + d_d \dot{x}_{c,3}(t)), \tag{16}$$

where $f'_{\text{ext},3}$ is the measured external force component along the contact axis Q_3, f_d is the desired scalar contact force, and $x_{c,3}$ is the admittance-generated command position along the same axis. The index $\varepsilon(t)$ represents the residual between the measured interaction force and the force predicted by the intended admittance dynamics. A small $|\varepsilon|$ indicates that the virtual admittance model is being rendered reliably, whereas a large $|\varepsilon|$ indicates rendering degradation.

This rendering-quality index is therefore used as a supervisory signal in the proposed FAAC. When $|\varepsilon|$ becomes large, the controller restricts aggressive mass adaptation by increasing the lower bound of the allowable mass range. This prevents the outer-loop admittance dynamics from entering an unsafe low-mass, high-bandwidth region that cannot be reliably rendered by the inner position-controlled robot.

4. Fuzzy-Based Adaptive Admittance Control

4.1. Overall Structure and Design Rationale

The proposed FAAC uses a set of fuzzy adaptation maps rather than a standalone fuzzy controller. This distinction is important because the fuzzy component does not directly generate a control input to the robot. Instead, it adapts the admittance parameters according to the observed interaction state. Specifically, FAAC consists of three fuzzy adaptation maps: the Mass-Adaptation Fuzzy Map (MAFM), the Damper–Mass Ratio Fuzzy Map (DMRFM), and the Rendering-Quality Supervisory Fuzzy Map (RQ-SFM).

The MAFM is the primary fuzzy map and determines the candidate increment of the dominant virtual mass eigenvalue $\Delta\lambda^*_{M,3}$. This map was not arbitrarily assigned; instead, it was designed through a simulator-guided procedure. Specifically, the contact response of the position-controlled robot was observed using a reduced-order discrete-time simulator, and the resulting transient behavior was partitioned in the force-error–force-error-derivative plane. For each partitioned region, the desired control objective was first interpreted in terms of force-control bandwidth and then translated into an increase or decrease in the virtual mass.

The DMRFM adapts the candidate increment of the damper–mass ratio Δr^*_{MD} rather than directly adapting the damping coefficient. This map was introduced because mass adaptation alone changes the damping-ratio behavior of the admittance dynamics. By coupling the damping eigenvalue with the mass eigenvalue through r_{MD}, the controller can adjust the stability–adaptability tradeoff in a more interpretable manner.

The RQ-SFM is a supervisory fuzzy map that constrains the allowable mass-adaptation range. The MAFM relies on force error and its derivative, but these signals do not fully represent rendering degradation in the cascade structure of a position-controlled robot. In particular, under high-stiffness contact, an excessive increase in the outer-loop force-control bandwidth can exceed the rendering capability of the inner position loop. Therefore, the RQ-SFM monitors the rendering-quality index and motion-level vibration, and generates the candidate lower-bound update $\Delta\lambda_s^*$ when unsafe rendering behavior is detected.

The fuzzy maps generate candidate parameter updates. These candidate updates are then passed through an energy-tank-based admissibility filter before being applied to the admittance model. Therefore, the fuzzy maps determine the desired direction of adaptation, while the energy tank determines whether the corresponding update is energetically admissible. This structure allows the proposed controller to improve force-tracking responsiveness while preserving passivity during online parameter adaptation and contact transitions.

The input and output ranges used for the fuzzy adaptation maps are summarized in Table 1. These ranges define the universes of discourse for the membership functions and the scaling of the adaptive outputs used throughout the proposed FAAC. To maintain consistent notation, $\Delta\lambda_{M,3}^*$ denotes the candidate increment of the dominant virtual mass eigenvalue generated by the MAFM, Δr_{MD}^* denotes the candidate increment of the damper–mass ratio generated by the DMRFM, and $\Delta\lambda_s^*$ denotes the candidate lower-bound adjustment generated by the RQ-SFM.

Table 1. Fuzzy input and output ranges used in the proposed FAAC.

Category	Symbol	Value	Description
Input	f_e	$[-5.5,\ 5.5]$	Force-error range for MAFM and DMRFM
Input	Δf_e	$[-1000,\ 1000]$	Force-error derivative range for MAFM and DMRFM
Input	ε	$[-5\times10^6,\ 5\times10^6]$	Rendering-quality index range for RQ-SFM
Input	$\mathrm{STD}(x_c - x)$	$[0,\ 2\times10^{-3}]$	Position-error standard deviation range for RQ-SFM
Output	$\Delta\lambda_{M,3}^*$	$[-0.5,\ 0.5]$	Candidate dominant-mass adaptation increment from MAFM
Output	Δr_{MD}^*	$[-2.5,\ 2.5]$	Candidate damper–mass ratio increment from DMRFM
Output	$\Delta\lambda_s^*$	$[-0.05,\ 0.05]$	Candidate lower-bound mass adjustment from RQ-SFM

All fuzzy maps use triangular membership functions with five linguistic values: NB (negative big), NS (negative small), ZE (zero), PS (positive small), and PB (positive big). A Mamdani-type inference system is used, and each crisp output is obtained by the center-of-gravity defuzzification method.

4.2. MAFM: Simulator-Guided Mass-Adaptation Fuzzy Map

4.2.1. Reduced-Order Simulation Model for Contact-Response Observation

The MAFM was designed by observing the contact response of a position-controlled robot in a reduced-order discrete-time simulator. The simulator was not intended to replace the full robot dynamics. Rather, it was used as a rule-design tool to capture the cascade interaction between the outer admittance loop and the inner position-control loop. The inner position loop of the UR10 was approximated as single-degree-of-freedom motor dynamics driven by a PD position controller, followed by the motor/inertial response and numerical integration to obtain the robot position. This reduced-order structure allows the main transient phenomena relevant to the force-control rule design to be observed with low complexity.

The simulated contact model consists of: (i) the reduced-order position-controlled robot dynamics; (ii) the admittance law

$$m_d\ddot{x}_c + d_d\dot{x}_c + k_d(x_c - x_d) = f_{\text{ext}} - f_d, \tag{17}$$

and (iii) a linear spring contact model

$$f_{\text{ext}} = k_e(x_d - x). \tag{18}$$

Here, x_c is the admittance-generated command position, x is the actual robot position generated by the inner position loop, x_d is the desired reference position, f_{ext} is the measured external force, f_d is the desired contact force, and k_e is the environment stiffness.

Rearranging Equation (17) gives

$$m_d\ddot{x}_c + d_d\dot{x}_c + k_d x_c = A(t), \tag{19}$$

where the aggregated admittance input is defined as

$$A(t) = k_d x_d(t) + f_{\text{ext}}(t) - f_d(t). \tag{20}$$

Applying a Tustin transform with sampling period T_s yields the following second-order difference equations:

$$x[t] = \sum_{i=0}^{2} \alpha_i x_c[t-i] - \sum_{j=1}^{2} \beta_j x[t-j]. \tag{21}$$

$$x_c[t] = \sum_{i=0}^{2} \gamma_i A[t-i] - \sum_{j=1}^{2} \delta_j x_c[t-j]. \tag{22}$$

Equation (21) represents the discretized inner position-loop response, whereas Equation (22) represents the discretized admittance dynamics. The position-loop coefficients $\{\alpha_i, \beta_j\}$ and admittance-law coefficients $\{\gamma_i, \delta_j\}$ are defined in Table 2.

Here, J and B denote the equivalent inertia and viscous coefficient of the reduced-order inner-loop model, respectively, and k_P and k_D are the proportional and derivative gains of the inner position controller. The gains are set as $\omega_n = 2\pi \cdot 166$ Hz, $\zeta = 1$, $k_P = \omega_n^2 J$, and $k_D = 2\zeta\omega_n J - B$. The simulation uses the following design parameters:

$$J = 1\ \text{kg} \cdot \text{m}^2,\ B = 10\ \text{N} \cdot \text{m} \cdot \text{s},\ m_d = 1\ \text{kg},\ d_d = 1000\ \text{N} \cdot \text{s/m},$$
$$k_d = 5000\ \text{N/m},\ k_e = 10{,}000\ \text{N/m},\ T_s = 2\ \text{ms}.$$

Each coefficient in Table 2 can be reproduced by substituting these values into the preceding formulas.

It should be emphasized that this reduced-order simulator is not used as an online plant model in the proposed controller. Instead, it is used only as a qualitative rule-design tool to observe the dominant transient tendencies of the cascade force-control structure. Therefore, the proposed FAAC does not require accurate identification of the robot inertia, viscous coefficient, inner-loop controller dynamics, or environment stiffness during online execution. The fuzzy adaptation maps use measured interaction signals, such as the force error, force-error derivative, rendering-quality index, and motion-level vibration, rather than model-predicted states. Consequently, moderate model mismatch mainly affects the offline rule-design interpretation and initial tuning, not the real-time adaptation law itself. In practical implementation, the membership ranges and scaling coefficients are further tuned in the actual control environment to account for unmodeled robot dynamics, actuator limits, sensor characteristics, pad compliance, friction, and contact nonlinearities.

Table 2. Position-loop and admittance-law coefficients.

Coefficient	Expression
A_{pos}	$4J + k_P T_s^2 - 2T_s(B + k_D)$
B_{pos}	$2k_P T_s^2 - 8J$
C_{pos}	$4J + k_P T_s^2 + 2T_s(B + k_D)$
D_{pos}	$k_P T_s^2 - 2T_s k_D$
E_{pos}	$2k_P T_s^2$
F_{pos}	$k_P T_s^2 + 2T_s k_D$
u_{Ad}	$4m_d - 2d_d T_s + k_d T_s^2$
v_{Ad}	$2k_d T_s^2 - 8m_d$
w_{Ad}	$4m_d + 2d_d T_s + k_d T_s^2$
α_0	$F_{\text{pos}}/C_{\text{pos}}$
α_1	$E_{\text{pos}}/C_{\text{pos}}$
α_2	$D_{\text{pos}}/C_{\text{pos}}$
β_1	$B_{\text{pos}}/C_{\text{pos}}$
β_2	$A_{\text{pos}}/C_{\text{pos}}$
γ_0	T_s^2/w_{Ad}
γ_1	$2T_s^2/w_{\text{Ad}}$
γ_2	T_s^2/w_{Ad}
δ_1	$v_{\text{Ad}}/w_{\text{Ad}}$
δ_2	$u_{\text{Ad}}/w_{\text{Ad}}$

4.2.2. Dynamic-State Partitioning in the Force-Error Plane

The MAFM was designed from the transient response observed in the simulator. The force error and its discrete-time derivative are defined as

$$f_e(t) = f_d(t) - f_{\text{ext}}(t), \tag{23}$$

$$\Delta f_e(t) = \frac{f_e(t) - f_e(t - T_s)}{T_s}. \tag{24}$$

The pair $(f_e, \Delta f_e)$ indicates not only the magnitude of the force-tracking error but also the direction in which the force response is evolving. Therefore, it provides an intuitive state representation for distinguishing whether the system is approaching the desired force, overshooting, moving toward a peak, recovering from a peak, or remaining near saturation.

Figure 2 illustrates how the transient contact-response regions are mapped to the MAFM input plane. The left panel shows the representative force response, force error, and force-error derivative used to define the dynamic regions A–I. The right panel shows the corresponding regions in the fuzzy input plane $(f_e, \Delta f_e)$ for MAFM design. These regions are not additional controller states; they are design partitions used to convert observed transient phenomena into fuzzy rules for $\Delta\lambda^*_{M,3}$. The labels A–I are used only for fuzzy-rule construction and are distinct from the parameter–environment scenarios discussed in Section 3.2.

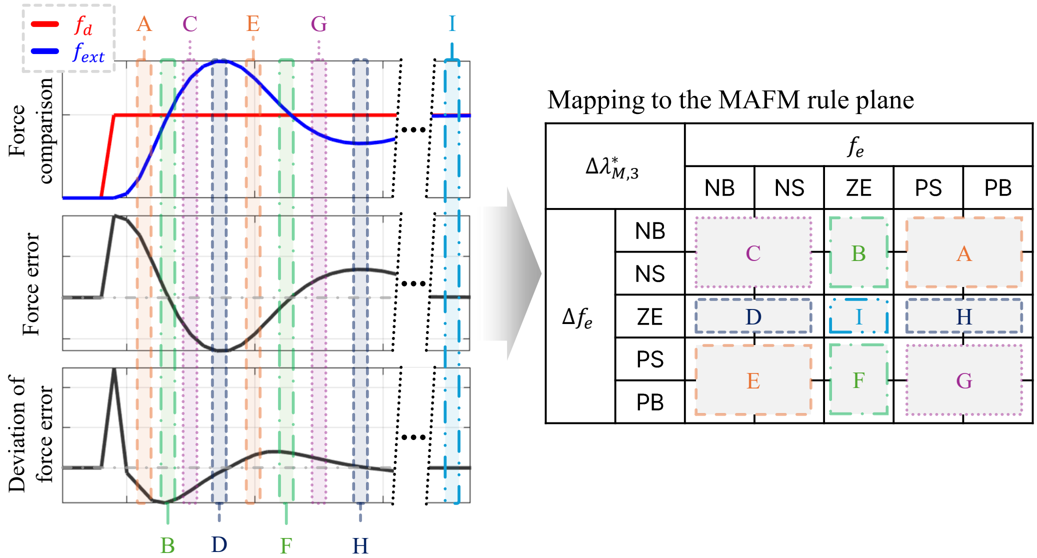

Figure 2. Mapping from contact-response regions to the MAFM rule plane. The left panel shows the representative transient response, force error, and force-error derivative used to define the dynamic regions A–I. The right panel shows the corresponding regions in the fuzzy input plane $(f_e, \Delta f_e)$ for MAFM design. The final linguistic outputs for the candidate mass increment $\Delta\lambda^*_{M,3}$ are assigned according to the bandwidth strategies summarized in Table 3. The labels A–I are used only for fuzzy-rule construction and are distinct from the parameter–environment scenarios discussed in Section 3.2.

The physical interpretation of each region is summarized in Table 3. The key design principle is that decreasing the virtual mass increases the effective admittance bandwidth and improves responsiveness, whereas increasing the virtual mass decreases the effective bandwidth and suppresses aggressive or oscillatory behavior. Thus, each transient region is first assigned a desired bandwidth behavior and then translated into a corresponding candidate mass-adaptation action.

Table 3. Dynamic-state interpretation for simulator-guided MAFM design. The region labels A–I correspond to the transient-response partitions in Figure 2 and are used only to translate observed transient phenomena into fuzzy mass-adaptation rules.

Region	Observed Situation	Control Objective	Bandwidth Strategy	Mass Action
A, E	Approaching the desired force	Maintain the current transient trend	No aggressive change	Small or zero update
B, F	Overshooting the desired force	Suppress overshoot and prevent oscillation	Decrease bandwidth	Increase M_d
C, G	Moving rapidly toward a force peak	Stabilize the transient response	Decrease bandwidth	Increase M_d
D, H	Near a force peak or reversal point	Recover adaptability after transient peak	Increase bandwidth	Decrease M_d
I	Near saturation or steady state	Avoid unnecessary parameter variation	Maintain bandwidth	Zero or small update

4.2.3. Translation into the MAFM Rule Base

The region-wise design objectives in Table 3 were translated into the MAFM rule table for $\Delta\lambda^*_{M,3}$. The mapping in Figure 2 explicitly connects the observed transient phenomena with the MAFM input plane. Thus, the MAFM rule table is obtained by first identifying the dynamic regions A–I, then assigning each region a bandwidth strategy in Table 3, and finally converting that strategy into a linguistic mass-increment output. The resulting MAFM rule table is summarized in Table 4.

For regions associated with overshoot or rapid motion toward a force peak, such as B, C, F, and G, the desired strategy is to decrease the effective force-control bandwidth. These regions are therefore assigned positive mass increments such as PS or PB, because increasing $\lambda_{M,3}$ suppresses aggressive transient behavior. For regions associated with recovery from a peak or the need for faster adaptation, such as D and H, the desired strategy is to increase the effective bandwidth. These regions are therefore assigned negative mass increments such as NS or NB. For regions close to saturation or steady-state behavior, such as I, the rule output is set to ZE or a small update to avoid unnecessary parameter variation.

A positive output increases the candidate virtual mass, thereby reducing the effective force-control bandwidth and improving transient stability. A negative output decreases the candidate virtual mass, thereby increasing the effective bandwidth and improving responsiveness. A zero output maintains the current mass value to prevent unnecessary parameter variation. Therefore, the MAFM rule table is not an arbitrary linguistic table; it is derived by converting the observed contact dynamics in Figure 2 and the region-wise strategies in Table 3 into bandwidth-oriented mass-adaptation rules.

The candidate mass update generated by the MAFM is expressed as

$$\lambda^*_{M,3}(t) = \lambda_{M,3}(t - T_s) + \Delta\lambda^*_{M,3}(t), \tag{25}$$

where $\Delta\lambda^*_{M,3}(t)$ is computed by the MAFM. This candidate update is not directly applied to the admittance model. Instead, the actually applied update is obtained after the energy-tank-based admissibility filter described in Section 4.5.

The virtual mass is constrained as

$$\lambda_s(t) \leq \lambda_{M,3}(t) \leq \lambda_b, \tag{26}$$

where λ_b is the upper bound of the virtual mass, and $\lambda_s(t)$ is the adaptive lower bound determined by the RQ-SFM described in Section 4.4.

Table 4. MAFM rule table for the candidate mass increment $\Delta\lambda^*_{M,3}$. The entries are derived from the dynamic-state mapping in Figure 2 and the bandwidth strategies summarized in Table 3.

$\Delta f_e \backslash f_e$	NB	NS	ZE	PS	PB
NB	PB	PB	PB	PB	ZE
NS	PS	PS	PS	ZE	NB
ZE	NB	NS	ZE	NS	NB
PS	NB	ZE	PS	PS	PS
PB	ZE	PB	PB	PB	PB

4.3. DMRFM: Coupled Damper–Mass Ratio Fuzzy Map

The MAFM changes the effective force-control bandwidth through $\lambda_{M,3}$. However, varying the virtual mass alone also changes the damping-ratio behavior of the admittance dynamics. If the damping eigenvalue is kept fixed while the mass changes, the transient response may become either underdamped or excessively sluggish depending on the contact condition. Therefore, the proposed FAAC adapts the damping eigenvalue in a coupled manner using the DMRFM.

Instead of directly updating $\lambda_{D,3}$, the dominant damping eigenvalue is updated as

$$\lambda_{D,3}(t) = r_{MD}(t)\, r_{IMD}\, \lambda_{M,3}(t), \tag{27}$$

$$r^*_{MD}(t) = r_{MD}(t - T_s) + \Delta r^*_{MD}(t), \tag{28}$$

where

$$r_{IMD} = \frac{\lambda_{D,3}(0)}{\lambda_{M,3}(0)}$$

is the initial damping-to-mass ratio at contact onset. The variable $r_{MD}(t)$ is a dimensionless scaling factor that modifies this initial ratio during contact. The candidate increment $\Delta r^*_{MD}(t)$ is produced by the DMRFM based on f_e and Δf_e, and the applied value $r_{MD}(t)$ is obtained after the energy-tank-based admissibility check. Here, the damper–mass ratio r_{MD} is the adaptive scaling variable used to update $\lambda_{D,3}$, whereas the damping ratio ζ denotes the dynamic damping ratio of the resulting second-order contact-axis response. This distinction is maintained throughout the manuscript to avoid confusion between the parameter-adaptation variable and the resulting dynamic response index.

The ratio-based approach is motivated by the distribution of the damping ratio ζ over the parameter space. As shown in Figure 3, when ζ is represented as a function of $(\lambda_{M,3}, \lambda_{D,3})$, the distribution exhibits only moderate planarity, with a plane-fitting coefficient of determination $R^2 = 0.839$. By contrast, when ζ is represented as a function of $(\lambda_{M,3}, r_{MD})$, the distribution becomes closer to a plane, with $R^2 = 0.9291$. This result does not directly indicate control performance; rather, it shows that the damping-ratio behavior is more nearly linear and predictable in the $(\lambda_{M,3}, r_{MD})$ domain. This property simplifies fuzzy rule-based design and enables a more intuitive trade-off between high adaptability and high stability.

The DMRFM follows two main principles. First, when Δf_e is large, the response is rapidly changing and may become oscillatory; therefore, r_{MD} is increased to enhance damping. Second, when f_e is large but Δf_e is relatively small, the response is slow; therefore, r_{MD} can be reduced to allow faster adaptation. The candidate increment Δr^*_{MD} is bounded as listed in Table 1, and the allowable range of r_{MD} is summarized in Table 7. The resulting DMRFM rule table is summarized in Table 5.

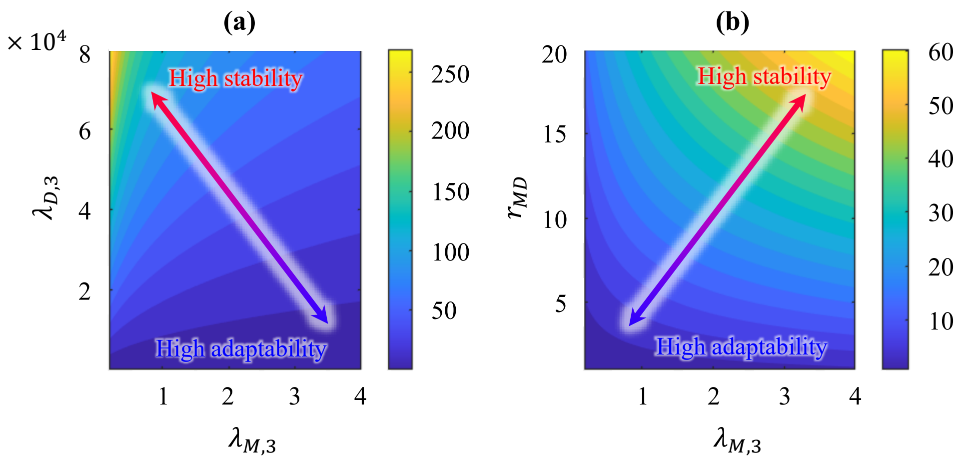

Figure 3. Comparison of damping-ratio distributions for two parameterizations. (**a**): ζ distribution in the $(\lambda_{M,3}, \lambda_{D,3})$ domain, with plane-fitting coefficient $R^2 = 0.839$. (**b**): ζ distribution in the $(\lambda_{M,3}, r_{MD})$ domain, with plane-fitting coefficient $R^2 = 0.9291$. The higher planarity in the ratio-based parameterization indicates that the damping-ratio behavior is more nearly linear and thus more suitable for DMRFM design.

Table 5. DMRFM rule table for Δr^*_{MD}.

$\Delta f_e \backslash f_e$	NB	NS	ZE	PS	PB
NB	PB	PB	PB	PB	PB
NS	PS	ZE	PS	ZE	PS
ZE	NB	NS	ZE	NS	NB
PS	PS	ZE	PS	ZE	PS
PB	PB	PB	PB	PB	PB

4.4. RQ-SFM: Rendering-Quality Supervisory Fuzzy Map

The MAFM and DMRFM improve responsiveness and transient stability under nominal rendering conditions. However, in a position-controlled robot, the outer admittance loop is implemented on top of the inner position-control loop. When the environment stiffness is high or when the outer-loop bandwidth becomes too large, the inner position loop may fail to accurately render the desired admittance dynamics. This cascade-induced degradation is not always detectable from the force error alone. Therefore, the RQ-SFM is introduced to constrain the lower bound of the virtual mass.

The RQ-SFM monitors two quantities. The first is the rendering-quality index ε from Equation (16), which measures the residual between the measured interaction force and the ideal admittance response. A large value of ε indicates that the rendered dynamics deviate from the intended admittance behavior. The second quantity is the standard deviation of the position error $\mathrm{STD}(x_c - x)$, computed over a finite sliding window. This metric captures motion-level vibration between the commanded admittance trajectory and the actual robot motion. The corresponding window size is given in Table 7.

Instead of directly overwriting the adapted mass, the RQ-SFM adjusts the lower bound $\lambda_s(t)$ of the allowable mass range. When rendering quality deteriorates, increasing λ_s prevents $\lambda_{M,3}$ from entering an unsafe low-mass region, thereby avoiding excessive force-control bandwidth. When both the rendering-quality index and the vibration metric recover, λ_s is decreased to restore the full adaptation range. This design preserves the freedom of the MAFM while blocking only the unsafe low-mass region.

The candidate lower-bound update is implemented as

$$\lambda_s^*(t) = \lambda_s(t - T_s) + \Delta\lambda_s^*(t), \tag{29}$$

where $\Delta\lambda_s^*(t)$ is computed by the RQ-SFM. The applied lower bound is determined through the energy-tank-based admissibility filter described in Section 4.5. The two main rules are as follows:

1. **Aggressive constraint:** if ε is high, increase λ_s to restrict mass adaptation and maintain stability.
2. **Full-range recovery:** if ε is low and $\mathrm{STD}(x_c - x)$ is low, decrease λ_s to recover the full mass-adaptation range.

These principles are implemented in the RQ-SFM rule table summarized in Table 6.

Table 6. RQ-SFM rule table for $\Delta\lambda_s^*$.

$\varepsilon \backslash \mathrm{STD}(x_c - x)$	NB	NS	ZE	PS	PB
NB	ZE	ZE	ZE	ZE	ZE
NS	ZE	ZE	ZE	ZE	ZE
ZE	ZE	ZE	NB	ZE	ZE
PS	ZE	ZE	PS	PS	PS
PB	ZE	ZE	PB	PB	PB

4.5. Energy-Tank-Based Admissibility and Passivity-Preserved Admittance Implementation

Energy-tank-based passivity mechanisms have been widely used to preserve stable robot interaction by storing dissipated energy and limiting active control actions [14,15]. The fuzzy maps generate candidate parameter updates, but these updates must satisfy both adaptive parameter bounds and energy-tank constraints before being applied to the admittance dynamics. For clarity, the bounds and tank-related parameters used in the proposed FAAC are summarized in Table 7 before the update laws are introduced. Here, λ_b denotes the upper bound of the adaptive mass range, i.e., $\lambda_b = \lambda_M^{\max}$.

Table 7. Adaptive bounds, contact-detection, tank-energy, and recovery parameters used in the proposed FAAC.

Category	Parameter	Value	Description
Adaptive bound	$\lambda_{M,3}$ range	[2, 10]	Allowable dominant mass eigenvalue range
Adaptive bound	r_{MD} range	[1, 20]	Allowable damper–mass ratio range
Adaptive bound	λ_s range	[2, 5]	Allowable lower-bound mass range
Contact logic	F_{contact}	2 N	Contact detection threshold
Contact logic	N_w	200 samples	Sliding-window size for STD$(x_c - x)$
Energy tank	$\mathcal{T}_{\min}$	0.2	Minimum usable tank energy
Energy tank	$\mathcal{T}_{\max}$	10	Maximum tank energy
Recovery	$\zeta_{\min}$	1	Minimum damping ratio for recovery
Recovery	$\lambda_{K,\epsilon}$	10^{-6}	Safeguarded stiffness lower bound for damping-ratio evaluation
Recovery	τ_{base}	1 s	Base recovery time constant
Recovery	$\tau_{\max}$	5 s	Maximum recovery time constant
Recovery	γ_D	5	Weight on damping-ratio effect
Recovery	ρ	10^{-3}	Small positive constant to avoid singularity in the logarithmic recovery law

4.5.1. Candidate Parameter Updates and Admissibility Filter

The three fuzzy maps generate candidate parameter updates according to the observed interaction state. However, these updates are not directly applied to the admittance model. Before application, they are passed through an energy-tank-based admissibility filter. This filter ensures that the time-varying admittance parameters do not inject more energy into the closed-loop system than is available in the tank.

Let the candidate outputs of the fuzzy maps be denoted by

$$\Delta\lambda_{M,3}^*(t), \quad \Delta r_{MD}^*(t), \quad \Delta\lambda_s^*(t), \tag{30}$$

where the superscript $(\cdot)^*$ denotes a candidate value before the passivity check. The corresponding candidate lower bound, mass, damper–mass ratio, and damping eigenvalue are computed as

$$\lambda_s^*(t) = \text{sat}_{[\lambda_s^{\min}, \lambda_s^{\max}]}\big(\lambda_s(t - T_s) + \Delta\lambda_s^*(t)\big), \tag{31}$$

$$\lambda_{M,3}^*(t) = \text{sat}_{[\lambda_s^*(t), \lambda_b]}\big(\lambda_{M,3}(t - T_s) + \Delta\lambda_{M,3}^*(t)\big), \tag{32}$$

$$r_{MD}^*(t) = \text{sat}_{[r_{MD}^{\min}, r_{MD}^{\max}]}\big(r_{MD}(t - T_s) + \Delta r_{MD}^*(t)\big), \tag{33}$$

$$\lambda_{D,3}^*(t) = r_{MD}^*(t) r_{IMD} \lambda_{M,3}^*(t). \tag{34}$$

Here, $\text{sat}_{[a,b]}(\cdot)$ denotes saturation within the interval $[a, b]$.

The candidate parameter update may create or consume energy because the admittance parameters are time-varying. In particular, the mass update induces the parametric power term

$$P_m^*(t) = \frac{1}{2}\dot{x}_c^T(t)\dot{M}_d^*(t)\dot{x}_c(t), \tag{35}$$

where $\dot{M}_d^*(t)$ is approximated from the candidate mass-adaptation update over one sampling period. For the dominant contact axis, this can be computed from

$$\dot{\lambda}_{M,3}^*(t) = \frac{\lambda_{M,3}^*(t) - \lambda_{M,3}(t - T_s)}{T_s}. \tag{36}$$

If the candidate update is dissipative or energy-neutral, it is fully allowed. If it requires active energy, it is allowed only when sufficient tank energy is available. This behavior is implemented using the scalar tank-based admissibility factor $\eta_T(t) \in [0, 1]$:

$$\eta_T(t) = \begin{cases} 1, & P_m^*(t) \le 0, \\ \mathrm{clamp}\left(\dfrac{\mathcal{T}(t) - \mathcal{T}_{\min}}{\mathcal{T}_{\max} - \mathcal{T}_{\min}}, 0, 1\right), & P_m^*(t) > 0, \end{cases} \tag{37}$$

where $\mathcal{T}(t)$ is the current tank energy, $\mathcal{T}_{\min}$ is the minimum usable energy threshold, and $\mathcal{T}_{\max}$ is the tank capacity. Thus, dissipative or energy-neutral updates are fully allowed, whereas energy-generating updates are gradually restricted when the tank energy becomes insufficient.

The actually applied parameters are then updated as

$$\lambda_s(t) = \lambda_s(t - T_s) + \eta_T(t)(\lambda_s^*(t) - \lambda_s(t - T_s)), \tag{38}$$

$$\lambda_{M,3}(t) = \lambda_{M,3}(t - T_s) + \eta_T(t)\big(\lambda_{M,3}^*(t) - \lambda_{M,3}(t - T_s)\big), \tag{39}$$

$$r_{MD}(t) = r_{MD}(t - T_s) + \eta_T(t)(r_{MD}^*(t) - r_{MD}(t - T_s)), \tag{40}$$

$$\lambda_{D,3}(t) = r_{MD}(t) r_{IMD} \lambda_{M,3}(t). \tag{41}$$

Therefore, the fuzzy maps determine the desired direction of adaptation, while the energy tank determines whether the corresponding parameter update is energetically admissible. In this sense, the tank acts as a passivity-preserving safety gate between the fuzzy adaptation maps and the admittance parameter update.

4.5.2. Energy-Tank Charging and Discharging Logic

The admissibility factor $\eta_T(t)$ limits the parameter update associated with time-varying mass, while the tank energy itself is updated by accumulating dissipated or returned energy and releasing only the available amount for active admittance behavior. To make this bookkeeping explicit, the tank-side update law and the corresponding charging/discharging logic are given below.

The scalar power flows used for tank bookkeeping are defined as

$$\begin{aligned} P_d &= \dot{x}_c^T D_d \dot{x}_c, & P_r &= \dot{x}_c^T K_d (x_r - x_c), \\ P_f &= -\dot{x}_c^T F_d, & P_m &= \tfrac{1}{2}\dot{x}_c^T \dot{M}_d \dot{x}_c. \end{aligned} \tag{42}$$

Here, P_d represents dissipated damping power, P_r represents the reference-related stiffness power, P_f represents the desired-force-related power, and P_m represents the parametric power induced by time-varying mass. The damping power P_d is nonnegative when D_d is positive definite and can be partially stored in the tank through $\alpha(\mathcal{T})$, whereas P_r, P_f, and P_m may either consume or return energy depending on their signs.

The tank energy is updated as

$$\dot{\mathcal{T}} = \alpha(\mathcal{T})P_d - \beta_r(\mathcal{T}, P_r)P_r - \beta_f(\mathcal{T}, P_f)P_f - \beta_m(\mathcal{T}, P_m)P_m, \tag{43}$$

where $\alpha(\mathcal{T})$ is a scalar function that determines how much dissipated damping power is stored in the tank, and $\beta_i(\mathcal{T}, P_i)$ is a scalar tank-side gate that determines whether the corresponding scalar power flow is allowed to charge or discharge the tank according to the current tank-energy level. The state-dependent scalar gating functions are defined as

$$\alpha(\mathcal{T}) = \begin{cases} 1, & \mathcal{T} < \mathcal{T}_{\min}, \\ \frac{1}{2}\left[1 + \cos\left(\pi \frac{\mathcal{T} - \mathcal{T}_{\min}}{\mathcal{T}_{\max} - \mathcal{T}_{\min}}\right)\right], & \mathcal{T}_{\min} \le \mathcal{T} \le \mathcal{T}_{\max}, \\ 0, & \mathcal{T} > \mathcal{T}_{\max}, \end{cases} \tag{44}$$

$$\beta_i(\mathcal{T}, P_i) = \begin{cases} 0, & (\mathcal{T} < \mathcal{T}_{\min} \wedge P_i > 0) \vee (\mathcal{T} > \mathcal{T}_{\max} \wedge P_i < 0), \\ 1, & \text{otherwise}, \end{cases} \tag{45}$$

for $i \in \{r, f, m\}$.

The corresponding scalar controller-side gate is defined as

$$\beta_i'(\mathcal{T}, P_i) = \begin{cases} 1, & \mathcal{T} \le \mathcal{T}_{\min} \wedge P_i < 0, \\ \beta_i(\mathcal{T}, P_i), & \text{otherwise}. \end{cases} \tag{46}$$

To make the energy bookkeeping explicit, Algorithm 1 summarizes the charging and discharging logic of the tank. The damping power P_d charges the tank through $\alpha(\mathcal{T})$, whereas P_r, P_f, and P_m either discharge or recharge the tank depending on their signs. The scalar tank-side gates β_i prevent the tank energy from leaving the admissible interval $[\mathcal{T}_{\min}, \mathcal{T}_{\max}]$.

Algorithm 1 Energy-Tank Charging and Discharging Logic

Compute the scalar power flows P_d, P_r, P_f, and P_m using Equation (42).
Compute the damping-energy storage gate $\alpha(\mathcal{T})$ using Equation (44).
for $i \in \{r, f, m\}$ **do**
    Compute the tank-side gate $\beta_i(\mathcal{T}, P_i)$ using Equation (45).
end for
Store dissipated damping energy: $\dot{\mathcal{T}} \leftarrow \alpha(\mathcal{T})P_d$.
for $i \in \{r, f, m\}$ **do**
    if $P_i > 0$ **then**
        The controller requests active energy from the tank.
        If $\beta_i = 1$, discharge the tank by P_i; otherwise, block the exchange.
    else if $P_i < 0$ **then**
        The controller returns energy to the tank.
        If $\beta_i = 1$, recharge the tank by $-P_i$; otherwise, block overcharging.
    else
        No tank exchange is required for this term.
    end if
    Accumulate the tank-energy rate: $\dot{\mathcal{T}} \leftarrow \dot{\mathcal{T}} - \beta_i P_i$.
end for
$\mathcal{T}(t + T_s) \leftarrow \mathrm{sat}_{[\mathcal{T}_{\min}, \mathcal{T}_{\max}]}\left(\mathcal{T}(t) + T_s\dot{\mathcal{T}}\right)$.

Thus, the tank accumulates dissipated or returned energy and releases only the available amount to support active admittance behavior. After the tank-side bookkeeping is completed, the corresponding controller-side gates β_i' are computed from Equation (46) and used to ensure that the energy allowed by the tank-side bookkeeping is consistently reflected in the passivity-preserved admittance dynamics.

4.5.3. Passivity-Preserved Admittance Controller

After the admissible admittance parameters are obtained and the controller-side gates are computed, the tank gates are applied to the admittance dynamics that generate the command motion. The resulting passivity-preserved admittance controller is written as

$$M_d(t)\ddot{x}_c(t) = F_{\text{ext}}(t) - D_d(t)\dot{x}_c(t) + \beta_r'(\mathcal{T}, P_r)K_d(t)(x_r(t) - x_c(t)) - \beta_f'(\mathcal{T}, P_f)F_d(t). \quad (47)$$

Here, β_r' and β_f' are scalar-valued controller-side gates associated with the scalar power flows P_r and P_f, respectively. Equation (47) represents the general passivity-preserved admittance form. During contact-force regulation in this study, the dominant-axis stiffness is set to zero, i.e., $\lambda_{K,3} = 0$, and therefore the reference-related term $K_d(t)(x_r(t) - x_c(t))$ vanishes along the contact axis. In this phase, the tank primarily regulates the desired-force-related driving term through β_f' and the time-varying mass/damping update through $\eta_T(t)$. The reference-related gate β_r' is retained in the formulation for completeness because it becomes relevant during non-contact motion, contact transition, or general admittance operation when the stiffness term is active. Although these gates multiply vector-valued effort terms in Equation (47), each gate uniformly scales the corresponding effort term according to the tank-energy condition. The tank does not directly scale the flow variable $\dot{x}_c$. Instead, it gates the effort-like terms that drive the admittance state and thereby shape $\ddot{x}_c$, $\dot{x}_c$, and x_c. The power associated with time-varying mass is regulated through the scalar admissibility factor $\eta_T(t)$ in Equations (38)–(41), which limits the effective variation of $M_d(t)$ and $D_d(t)$ before they are used in Equation (47). Therefore, the energy tank is coupled to the admittance controller in two ways: it gates the explicit admittance-driving terms through the scalar controller-side gates β_i' and restricts the implicit parametric energy variation through the scalar update gate $\eta_T(t)$.

4.6. Contact Transition Strategy

During contact, the proposed FAAC continuously adapts $\lambda_{M,3}$, $\lambda_{D,3}$, and $\lambda_{K,3}$ according to the interaction state. However, when the contact state changes, the parameters adapted for the previous contact condition may become unsuitable for the next interaction. For example, if the commanded force goes to zero or a new contact begins, retaining the previously adapted parameters can generate an undesirable transient response. Therefore, the admittance parameter $\lambda_{\Sigma,3}$ is smoothly recovered toward its nominal value $\lambda_{\Sigma,\text{nom}}$.

A direct parameter reset can inject energy into the closed-loop system. To avoid this issue, the recovery is implemented as a passivity-aware exponential update:

$$\lambda_{\Sigma,3}(t + T_s) = \lambda_{\Sigma,3}(t) + \frac{T_s}{\tau_{\text{dyn}}(t)}\big(\lambda_{\Sigma,\text{nom}} - \lambda_{\Sigma,3}(t)\big). \quad (48)$$

This procedure is summarized in Algorithm 2.

Algorithm 2 Parameter Recovery at Contact Transition

1: **if** $F_d(t) \neq 0$ **then**
2: Set $\lambda_{K,3} \leftarrow 0$ and record $\lambda_{\Sigma,\text{start}} = \lambda_{\Sigma,3}(t)$.
3: **else if** $\lambda_{\Sigma,3}(t) \neq \lambda_{\Sigma,\text{start}}$ **then**
4: Compute the tank-based scale $\sigma(t)$ via Equation (49).
5: Compute the safeguarded damping-ratio scale $\phi(t)$ via Equation (52).
6: Compute the recovery time constant $\tau_{\text{dyn}}(t)$ via Equation (53).
7: **end if**

The recovery speed is determined by the dynamic time constant $\tau_{\text{dyn}}(t)$, which depends on the energy available in the tank and the instantaneous damping-ratio condition. First, the tank-based scale is defined as

$$\sigma(t) = \text{clamp}\Big(\frac{\mathcal{T}(t) - \mathcal{T}_{\min}}{\mathcal{T}_{\max} - \mathcal{T}_{\min}}, 0, 1\Big), \tag{49}$$

where $\mathcal{T}(t)$ is the current tank energy, $\mathcal{T}_{\min}$ is the minimum usable energy threshold, and $\mathcal{T}_{\max}$ is the tank capacity. A larger $\sigma(t)$ indicates that more usable energy is available, allowing faster parameter recovery. A smaller $\sigma(t)$ slows the recovery to avoid excessive energy consumption.

To avoid singularity when $\lambda_{K,3}(t)$ becomes zero or approaches zero during the transition, we introduce a safeguarded stiffness

$$\lambda^{\text{eff}}_{K,3}(t) = \max\big(\lambda_{K,3}(t),\ \lambda_{K,\epsilon}\big), \tag{50}$$

where $\lambda_{K,\epsilon} > 0$ is a small design constant. The instantaneous damping ratio is then evaluated as

$$\zeta(t) = \frac{\lambda_{D,3}(t)}{2\sqrt{\lambda_{M,3}(t)\lambda^{\text{eff}}_{K,3}(t)}}, \tag{51}$$

and the underdamping penalty scale is defined as

$$\phi(t) = \text{clamp}\Big(\frac{\zeta_{\min} - \zeta(t)}{\zeta_{\min}}, 0, 1\Big), \tag{52}$$

where $\zeta_{\min}$ is the minimum acceptable damping ratio. When the system becomes underdamped, $\phi(t)$ increases and slows the parameter recovery.

Finally, the recovery time constant is computed as

$$\tau_{\text{dyn}}(t) = \min\Big\{\tau_{\text{base}} \ln\big(\tfrac{1}{\sigma(t)} + \rho\big)\big(1 + \gamma_D \phi(t)\big),\ \tau_{\max}\Big\}, \tag{53}$$

where τ_{base}, ρ, γ_D, and $\tau_{\max}$ are design constants. This formulation allows fast recovery when sufficient tank energy and damping are available, while slowing the transition when energy is limited or the system is close to an underdamped condition.

Therefore, the energy tank affects the proposed controller in two ways. During continuous contact, it scales or blocks fuzzy-map-based parameter updates through the admissibility factor $\eta_T(t)$. During contact transitions, it regulates the nominal-parameter recovery speed through the tank-based scale $\sigma(t)$ in $\tau_{\text{dyn}}(t)$. In both cases, the energy tank prevents abrupt parameter changes from injecting unbounded active energy into the closed-loop interaction.

4.7. Passivity Analysis of the Energy-Tank-Coupled Admittance System

The tank charging/discharging logic and the passivity-preserved admittance controller were introduced in Section 4.5. This section analyzes the passivity of the resulting energy-tank-coupled admittance system. The analysis focuses on the power balance between the controller-side storage and the tank-side energy bookkeeping.

The storage function for the admittance dynamics is defined as

$$V = \tfrac{1}{2}\dot{x}_c^T M_d \dot{x}_c. \tag{54}$$

Using the scalar power flows defined in Equation (42), the controller-side modified stored-energy rate associated with the passivity-preserved admittance dynamics can be written as

$$\begin{aligned}\dot{V}' = {} & \dot{x}_c^T F_{\text{ext}} - P_d \\ & + \beta_r'(\mathcal{T}, P_r)P_r + \beta_f'(\mathcal{T}, P_f)P_f + \beta_m'(\mathcal{T}, P_m)P_m.\end{aligned} \tag{55}$$

Here, β_m' is a scalar controller-side gate associated with the scalar parametric power induced by time-varying mass. In implementation, this parametric contribution is restricted through the scalar admissibility factor $\eta_T(t)$ in Equations (38)–(41); in the passivity analysis, it is represented as the gated power term $\beta_m' P_m$.

The tank-side energy bookkeeping is given by Equation (43). The roles of β_i and β_i' are different but complementary. The coefficient $\beta_i(\mathcal{T}, P_i)$ is the scalar tank-side gate, which determines whether the corresponding power flow is allowed to charge or discharge the tank. In contrast, $\beta_i'(\mathcal{T}, P_i)$ is the scalar controller-side gate, which determines how much of the corresponding power contribution is reflected in the modified controller storage rate $\dot{V}'$ and in the passivity-preserved admittance dynamics. Thus, the tank-side term $-\beta_i P_i$ in $\dot{\mathcal{T}}$ and the controller-side term $+\beta_i' P_i$ in $\dot{V}'$ describe the same internal power exchange from opposite sides. When the exchange is admissible, the energy released from or absorbed by the tank is consistently reflected in the controller-side dynamics. When the tank energy is insufficient, the controller-side gate prevents the controller from using unavailable active energy. Therefore, the internal power exchange is canceled or restricted so that no net active energy is generated by the controller–tank interconnection.

Combining Equations (55) and (43) yields

$$\dot{V}' + \dot{\mathcal{T}} \leq \dot{x}_c^T F_{\text{ext}}. \tag{56}$$

Since $\mathcal{T}(t)$ is lower bounded by $\mathcal{T}_{\min}$, the total storage function $V' + \mathcal{T}$ remains bounded from below. Therefore, the closed-loop admittance system is passive with respect to the external port $(F_{\text{ext}}, \dot{x}_c)$ under all admissible parameter updates and contact transitions.

4.8. Simulation-Based Comparative Analysis

To examine the effectiveness of the proposed controller before hardware experiments, we conducted comparative simulations under different sensing conditions. The simulations were implemented in MATLAB R2024b using a custom script-based simulator derived from the discrete-time equations in Section 4.2. Simulink was not used. This simulation study was designed as an ablation and robustness analysis. Therefore, it focuses on two objectives. The first objective is to verify the contribution of each adaptation component. The second objective is to evaluate robustness under sensing uncertainty and filter-induced delay. The hardware experiment in Section 5 validates the complete FAAC framework in a real polishing task.

The proposed full FAAC was compared with two baseline controllers. The first baseline is a classical adaptive admittance controller (AAC). This controller updates the admittance stiffness parameter online based on a previously reported adaptive admittance strategy [16]. The second baseline is an ablated version of the proposed method, denoted as FAAC-M. FAAC-M uses the Mass-Adaptation Fuzzy Map (MAFM) to adapt the virtual mass according to the dynamic contact state. In this baseline, the damping coefficient is not fixed. Instead, it is updated proportionally to the adapted mass using a constant damper–mass ratio. Thus, FAAC-M performs coupled mass–damping adaptation with a fixed damping-ratio structure. However, it excludes the Damper–Mass Ratio Fuzzy Map (DMRFM), the Rendering-Quality Supervisory Fuzzy Map (RQ-SFM), and the energy-tank-based admissibility filter. This baseline is included to verify whether fixed-ratio mass–damping adaptation is sufficient. It also clarifies whether the complete FAAC architecture is necessary. The complete architecture includes fuzzy damping-ratio regulation, rendering-quality supervision, and energy-tank-based admissibility.

The simulations were performed under three sensing conditions. To avoid confusion with the parameter–environment scenarios discussed in Section 3.2, the labels Case A–Case C are used here only to denote sensing conditions for the simulation study. They do not denote the admittance-parameter scenarios or the comparison algorithms. Case A represents the nominal condition without additional sensing issues. Case B evaluates the effect of force-sensor noise by adding sensor noise with a magnitude of 2 N to the measured force signal. Case C evaluates the effect of force-signal filtering by applying a low-pass filter with a cutoff frequency of 50 Hz. These cases are summarized in Table 8. The purpose of these cases is to evaluate nominal force-tracking performance. They also evaluate the practical trade-off between sensor-noise reduction and filter-induced degradation of force-control quality.

Table 8. Simulation sensing conditions and compared controllers for ablation and robustness analysis. Case A–Case C denote sensing conditions only and are different from the parameter–environment scenarios in Section 3.2.

Case	Sensing Condition	Purpose
A	No additional sensing issue	Nominal comparison under ideal force feedback
B	Force-sensor noise with magnitude of 2 N	Robustness evaluation under noisy force measurement and motivation for filtering
C	Low-pass-filtered force feedback with cutoff frequency of 50 Hz	Evaluation of filter-induced delay and control-quality degradation

For readability, the simulation results are presented in three separate figures, one for each sensing condition. In all figures, rows (1)–(3) correspond to AAC, FAAC-M, and the proposed full FAAC, respectively. Thus, Case A–Case C indicate sensing conditions, whereas rows (1)–(3) indicate the compared controllers. The three columns correspond to different contact stiffness values. The desired force F_d and the measured external force F_{ext} are compared to evaluate convergence, overshoot, divergence, and force-tracking consistency.

Figure 4 shows the nominal simulation results under Case A. No additional sensing issue is considered in this case. Under this condition, AAC improves steady-state force tracking by adapting the stiffness parameter. However, it still exhibits overshoot or degraded transient behavior under challenging contact conditions. FAAC-M improves the response by adapting the virtual mass through MAFM. It also updates the damping coefficient proportionally according to a constant damper–mass ratio. This coupled mass–damping adaptation provides a more balanced transient response than stiffness-only adaptation. The reason is that the damping level changes together with the adapted mass. However, FAAC-M still uses a fixed damper–mass ratio. It also does not include rendering-quality supervision or energy-tank-based admissibility. In contrast, the proposed full FAAC achieves more reliable force tracking by coordinating mass adaptation, damper–mass ratio adaptation, rendering-quality supervision, and energy-tank-based admissibility filtering.

Figure 5 shows the simulation results under Case B. In this case, force-sensor noise with a magnitude of 2 N is added to the measured force signal. This condition evaluates how noise affects the fuzzy-map inputs and the resulting force-control behavior. Under noisy sensing, AAC becomes more sensitive to force fluctuations because the stiffness update directly responds to the noisy force signal. FAAC-M and the proposed full FAAC maintain bounded responses. This is because mass adaptation reduces overly aggressive transients and the damping coefficient is coupled with the mass. However, noisy force feedback can still perturb the adaptation signals and degrade smooth parameter evolution. Therefore, Case B also motivates the practical use of force-signal filtering in real implementations.

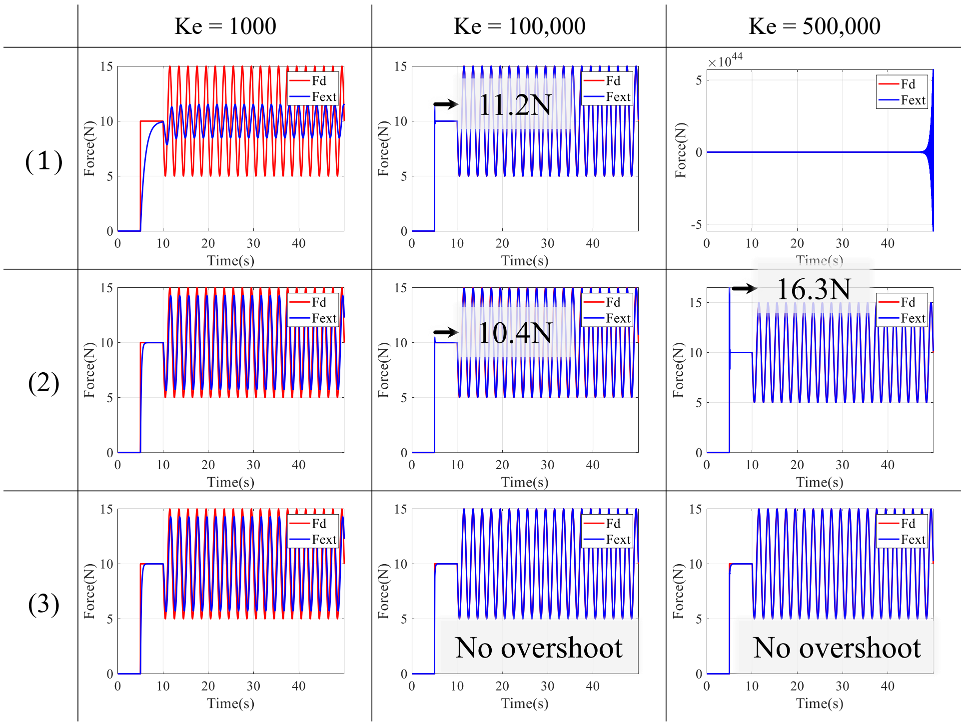

Figure 4. Comparative simulation results under the nominal sensing condition without additional sensing issues. Rows (1)–(3) correspond to AAC, FAAC-M using the Mass-Adaptation Fuzzy Map with a constant damper–mass ratio, and the proposed full FAAC, respectively. The three columns correspond to different contact stiffness values.

Figure 6 shows the simulation results under Case C. In this case, the measured force signal is filtered using a low-pass filter with a cutoff frequency of 50 Hz. This case was included because the noisy condition in Case B indicates the practical need for noise reduction. Although low-pass filtering attenuates sensor noise, it also introduces phase delay into the force feedback used by the outer admittance loop. This delay degrades the rendering quality of the cascade structure composed of the outer admittance loop and the inner position loop.

The effect is particularly critical for FAAC-M. FAAC-M adapts the mass and damping through a fixed damper–mass ratio without explicitly monitoring rendering degradation. Therefore, when filtered feedback causes phase delay, FAAC-M can continue to select a responsive low-mass region. It can also maintain proportionally reduced damping without recognizing that the rendered admittance dynamics have become unreliable. As a result, FAAC-M can exhibit excessive overshoot or unstable transient behavior under filtered sensing.

The proposed full FAAC mitigates this problem by using the RQ-SFM. The RQ-SFM monitors rendering quality and motion-level vibration. It also restricts unsafe low-mass adaptation when the rendered admittance dynamics become unreliable. In addition, DMRFM allows the damping-ratio behavior to be adjusted according to the interaction state. Thus, the proposed controller is not constrained to a constant-ratio relationship. Therefore, the full FAAC addresses the practical trade-off between noise reduction and filter-induced control-quality degradation.

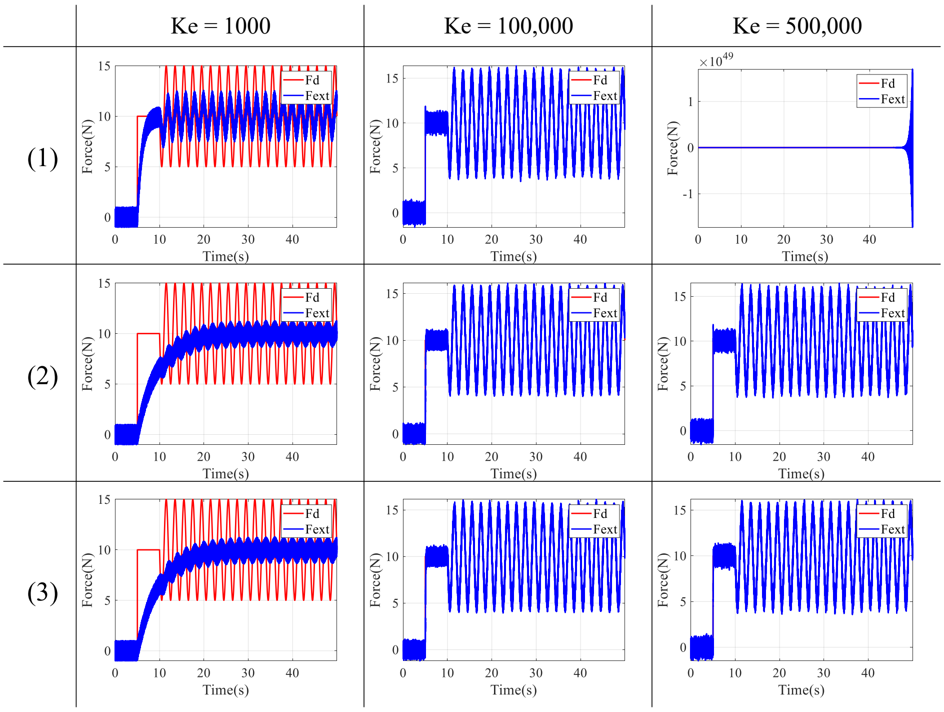

Figure 5. Comparative simulation results under noisy sensing. Force-sensor noise with a magnitude of 2 N is added to the measured force signal. Rows (1)–(3) correspond to AAC, FAAC-M, and the proposed full FAAC, respectively. The three columns correspond to different contact stiffness values. Both FAAC-M and the proposed full FAAC maintain bounded responses under noisy force feedback, whereas AAC is more sensitive to noise-induced fluctuation.

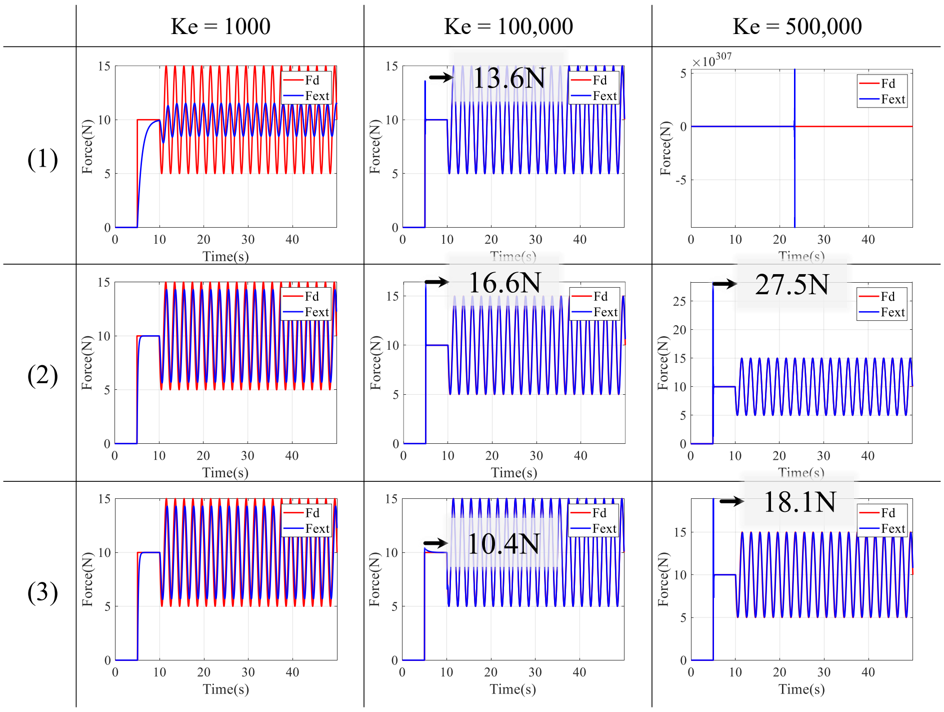

Figure 6. Comparative simulation results under filtered sensing. The measured force signal is filtered using a low-pass filter with a cutoff frequency of 50 Hz. Rows (1)–(3) correspond to AAC, FAAC-M, and the proposed full FAAC, respectively. The three columns correspond to different contact stiffness values. The proposed full FAAC better preserves force-tracking quality under filter-induced delay, whereas the baselines exhibit larger overshoot or unstable transient behavior.

Taken together, the noisy and filtered sensing conditions, Case B and Case C, reveal an important practical trade-off in force-feedback-based admittance adaptation. Noisy force measurements can perturb the fuzzy-map inputs and weaken smooth adaptation. This motivates the use of force-signal filtering. However, filtering introduces feedback delay and can degrade the rendering quality of a cascade admittance structure. The ablation result shows that fixed-ratio mass–damping adaptation improves the response compared with stiffness-only adaptation. However, it is still insufficient to handle the combined effects of sensing noise, filter-induced delay, and rendering-quality degradation. The proposed full FAAC addresses this issue by combining dynamic-phenomenon-driven mass adaptation, fuzzy damping-ratio regulation, rendering-quality supervision, and energy-tank-based admissibility filtering. Therefore, the proposed architecture provides more robust force tracking than both stiffness-only adaptation and fixed-ratio mass–damping adaptation under nominal, noisy, and filtered sensing conditions.

5. Experimental Validation

5.1. Experimental Setup

To evaluate the adaptability and stability of the proposed controller, polishing experiments were conducted using four controllers. The compared controllers were two baseline adaptive admittance controller settings, an ablated mass–damping adaptive baseline, and the proposed full FAAC. The two baseline settings are denoted as AAC 1 and AAC 2. The ablated mass–damping adaptive baseline is denoted as FAAC-M.

In AAC 1 and AAC 2, the admittance stiffness was updated online according to a conventional adaptive-admittance strategy. The virtual mass and damping were fixed. Specifically, AAC 1 and AAC 2 used $(M_d, D_d) = (0.5, 1000)$ and $(3, 6000)$, respectively.

FAAC-M was included as an ablated mass–damping adaptive baseline. It adapts the virtual mass according to the force-tracking state and updates the damping coefficient using a constant damper–mass ratio. However, unlike the proposed full FAAC, FAAC-M does not include fuzzy damper–mass ratio adaptation, rendering-quality supervision, or energy-tank-based admissibility filtering. In contrast, the proposed FAAC adaptively regulates the dominant mass and damping-related parameters. It also constrains unsafe adaptation through rendering-quality supervision and energy-tank-based admissibility.

As shown in Figure 7, the experimental setup comprises the following:

- A UR10 manipulator with a 10 kg payload;
- An AIDIN AFT200-D80 6-axis force/torque sensor;
- A wool polishing wheel mounted at the flange;
- An automotive fender segment as the workpiece.

Instead of using a fully dense surface path, a sparse set of discrete teaching points was defined on the workpiece surface. The polishing trajectory was then generated by linear interpolation between these points. All controllers were implemented at a 500 Hz control loop.

The UR10 was operated through its built-in position-control interface. The proposed FAAC was implemented as an outer-loop admittance controller. It generated position commands for this interface.

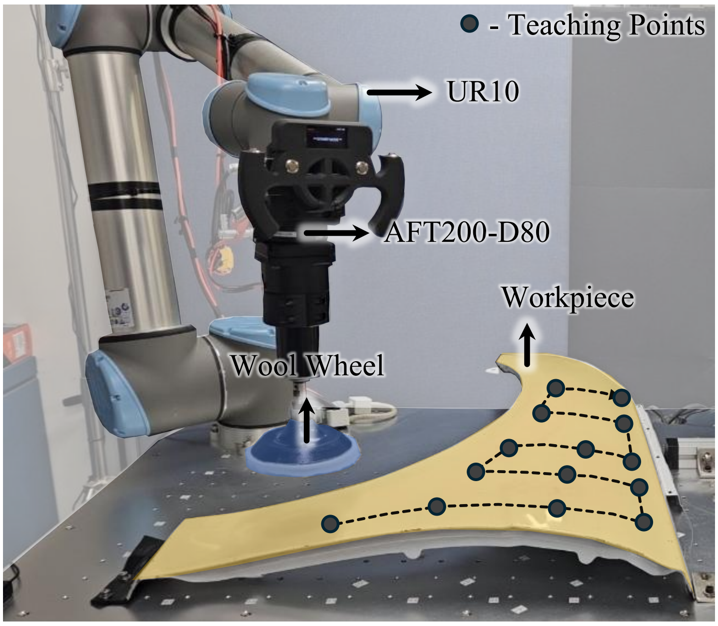

Figure 7. Experimental setup: UR10 with AFT200-D80 and a wool-polishing wheel polishing an automotive fender. Black-dotted points indicate teaching points used to generate the polishing trajectory.

5.2. Experimental Results

Figure 8 compares the force-tracking and parameter-adaptation profiles of AAC 1, AAC 2, FAAC-M, and the proposed FAAC during the polishing task. Here, AAC 1, AAC 2, FAAC-M, and Proposed FAAC denote the compared controllers in the experiment and should not be confused with the parameter–environment scenarios in Section 3.2 or the sensing-condition cases in the simulation study. The desired contact force was 20 N. In AAC 1 and AAC 2, the virtual mass and damping remained fixed while the desired stiffness was adaptively updated. Therefore, the force response depended strongly on the selected fixed mass–damping setting and on the transient behavior of the stiffness update.

AAC 1 used a relatively small virtual mass and damping value. This setting provided a more responsive contact behavior than AAC 2, but it also produced repeated force fluctuations. In particular, the desired stiffness profile of AAC 1 shows abrupt changes during continuous contact. These sudden stiffness changes are closely associated with transient force drops and contact-loss events. AAC 2 used a larger fixed mass and damping value. However, simply increasing the fixed mass and damping did not guarantee stable force regulation. AAC 2 exhibited the largest force variation, with a maximum force of 59.8 N and a force standard deviation of 11.28 N. Similar to AAC 1, the abrupt desired stiffness changes in AAC 2 were accompanied by unstable contact behavior.

FAAC-M improved contact maintenance compared with AAC 1 and AAC 2 by adapting the mass and updating the damping coefficient through a constant damper–mass ratio. As a result, FAAC-M eliminated jumping events and reduced the force standard deviation to 3.37 N. However, because FAAC-M does not include fuzzy damper–mass ratio adaptation, rendering-quality supervision, or energy-tank-based admissibility filtering, its force variation remained larger than that of the proposed full FAAC.

In contrast, the proposed FAAC maintained the most consistent force response during continuous polishing. The proposed method suppressed abrupt contact instability by coordinating mass adaptation, damping-related adaptation, stiffness behavior, and passivity-aware admissibility. As summarized in Table 9, the proposed FAAC achieved the highest minimum contact force of 13.5 N, the lowest maximum force of 31.7 N, and the smallest force standard deviation of 2.76 N among all compared methods. In addition, the proposed

FAAC showed zero jumping events, indicating more reliable maintenance of continuous surface contact.

These experimental results demonstrate that the proposed FAAC improves both force-tracking consistency and contact-maintenance robustness compared with the fixed-parameter AAC baselines and the ablated FAAC-M baseline. The results also indicate that contact instability in the baseline AAC controllers is related not only to the fixed mass–damping selection but also to abrupt stiffness changes during contact.

Table 9. Quantitative comparison of force-tracking performance and contact-maintenance robustness in the polishing experiment.

Algorithms	AAC 1	AAC 2	FAAC-M	Proposed FAAC
Min. Force (N)	0.7	0.7	7.5	13.5
Max. Force (N)	32.7	59.8	38.5	31.7
Force STD (N)	4.08	11.28	3.37	2.76
# of Jumping	2	1	0	0

Note: # of Jumping denotes the number of times that the robot detached from the surface during continuous contact control.

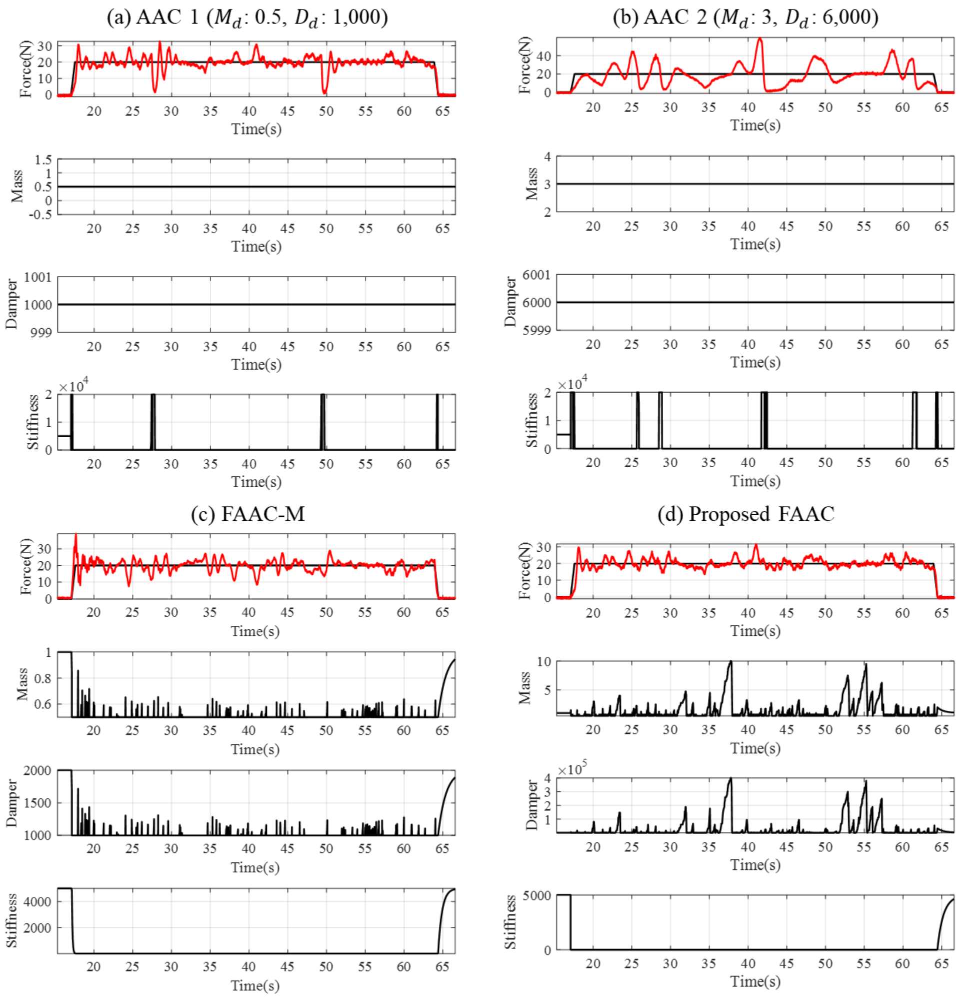

Figure 8. Force-tracking and parameter-adaptation profiles of (**a**) AAC 1 with $(M_d, D_d) = (0.5, 1000)$, (**b**) AAC 2 with $(M_d, D_d) = (3, 6000)$, (**c**) FAAC-M, and (**d**) the proposed FAAC during the polishing task. The plots show the measured contact force and the corresponding desired stiffness, mass, and damping profiles. The labels (**a**–**d**) denote the compared controllers, not the parameter–environment scenarios discussed in Section 3.2 or the sensing-condition cases in Section 4.8.

6. Conclusions

This paper proposed a fuzzy-based adaptive admittance controller for uncertain contact environments. The proposed method adapts the dominant-axis virtual mass and damping-related parameters within valid rendering regions. It also restricts adaptation in low-rendering-quality regions to preserve stability. The MAFM improves responsiveness or suppresses aggressive transients according to the force-tracking state. The DMRFM adjusts the damper–mass ratio to regulate the stability–adaptability trade-off. In addition, the RQ-SFM constrains unsafe low-mass adaptation by monitoring the rendering-quality index and motion-level vibration.

An energy-tank-based admissibility filter was integrated between the fuzzy adaptation maps and the passivity-preserved admittance controller. This filter prevents energetically inadmissible parameter updates during online adaptation and contact transitions. The resulting framework improves force-tracking performance while maintaining passivity of the admittance interaction.

Both simulation and experimental results confirmed the effectiveness of the proposed FAAC. In simulation, the proposed full FAAC provided more robust force tracking than both the stiffness-adaptive AAC baseline and the ablated mass–damping adaptive baseline. This improvement was observed under nominal, noisy, and low-pass-filtered force-feedback conditions. These results indicate that fixed-ratio mass–damping adaptation improves the response compared with stiffness-only adaptation. However, it remains insufficient when sensing noise, filter-induced delay, and rendering-quality degradation occur simultaneously.

In the polishing experiment, the proposed FAAC achieved the most consistent force response among all compared methods. Compared with AAC 1, AAC 2, and FAAC-M, the proposed FAAC achieved the highest minimum contact force of 13.5 N. It also achieved the lowest maximum force of 31.7 N and the smallest force standard deviation of 2.76 N. In addition, it eliminated contact-loss events during continuous surface interaction. In contrast, the baseline AAC controllers exhibited contact-loss events. Their force drops were associated with abrupt stiffness changes during contact. These results demonstrate that the proposed FAAC improves force-tracking consistency and contact-maintenance robustness in practical polishing tasks.

As a future extension, the proposed FAAC may also support impedance-learning or reinforcement-learning-based contact control [10,11]. FAAC enables stable force interaction under uncertain contact conditions. Therefore, it can provide a practical way to collect real-robot contact transition data for pre-training or offline policy learning. A learned policy can provide nominal impedance or admittance behaviors. Meanwhile, FAAC can refine the dominant mass and damping parameters online. It can also restrict unsafe updates through the energy-tank-based admissibility filter. In this way, FAAC can serve as a low-level passivity-preserving adaptation layer for learning-based contact controllers in unknown environments.

Author Contributions: Conceptualization, J.S. (Jaeyun Sim) and H.R.C.; methodology, J.S. (Jaeyun Sim), Y.K. and E.-C.K.; software, J.S. (Jaeyun Sim) and E.S.; validation, J.S. (Jaeyun Sim), Y.K. and S.L.; formal analysis, J.S. (Jaeyun Sim) and J.S. (Jaeyoon Sim); investigation, all authors; resources, H.R.C.; data curation, J.S. (Jaeyun Sim) and E.S.; writing—original draft preparation, J.S. (Jaeyun Sim); writing—review and editing, all authors; visualization, J.S. (Jaeyun Sim) and E.S.; supervision, H.R.C.; project administration, H.R.C. All authors have read and agreed to the published version of the manuscript.

Funding: This research was supported by the Ministry of Trade, Industry and Energy (MOTIE), Republic of Korea, under Project No. P0026249.

Institutional Review Board Statement: Not applicable.

Informed Consent Statement: Not applicable.

Data Availability Statement: The data presented in this study are available from the corresponding author upon reasonable request.

Acknowledgments: The authors thank the members of the robotics laboratory at Sungkyunkwan University for their technical support during the experimental setup and validation.

Conflicts of Interest: The authors declare no conflicts of interest.

References

1. Samuel, K.; Haninger, K.; Oboe, R.; Oh, S. Outer-Loop Admittance and Motion Control Dual Improvement via a Multi-Function Observer. *IEEE Trans. Ind. Electron.* **2024**, *71*, 9339–9350. [CrossRef]
2. Zhang, H.; Li, L.; Zhao, J.; Zhao, J. The hybrid force/position anti-disturbance control strategy for robot abrasive belt grinding of aviation blade based on fuzzy PID control. *Int. J. Adv. Manuf. Technol.* **2021**, *114*, 3645–3656. [CrossRef]
3. Hogan, N. Impedance Control: An Approach to Manipulation: Part II—Implementation. *J. Dyn. Syst. Meas. Control* **1985**, *107*, 8–16. [CrossRef]
4. Shen, Y.; Lu, Y.; Zhuang, C. A fuzzy-based impedance control for force tracking in unknown environment. *J. Mech. Sci. Technol.* **2022**, *36*, 5231–5242. [CrossRef]
5. Wu, Q.; Wang, Z.; Chen, Y.; Wu, H. Barrier Lyapunov Function-Based Fuzzy Adaptive Admittance Control of an Upper Limb Exoskeleton Using RBFNN Compensation. *IEEE/ASME Trans. Mechatron.* **2025**, *30*, 3–14. [CrossRef]
6. Duan, J.; Gan, Y.; Chen, M.; Dai, X. Adaptive Variable Impedance Control for Dynamic Contact Force Tracking in Uncertain Environment. *Robot. Auton. Syst.* **2018**, *102*, 54–65. [CrossRef]
7. Jin, Z.; Qin, D.; Liu, A.; Zhang, W.; Yu, L. Model Predictive Variable Impedance Control of Manipulators for Adaptive Precision-Compliance Tradeoff. *IEEE/ASME Trans. Mechatron.* **2023**, *28*, 1174–1186. [CrossRef]
8. Wu, H.; Yang, J.; Huang, S.; Li, J. Adaptive Optimal Admittance Control for Robotic Precision Grinding Based on Improved Normalized Advantage Function. *IEEE/ASME Trans. Mechatron.* **2025**, *30*, 5166–5178. [CrossRef]
9. Hu, X.; Liu, G.; Ren, P.; Jia, B.; Liang, Y.; Li, L.; Duan, S. An Admittance Parameter Optimization Method Based on Reinforcement Learning for Robot Force Control. *Actuators* **2024**, *13*, 354. [CrossRef]
10. Xing, X.; Burdet, E.; Si, W.; Yang, C.; Li, Y. Impedance learning for human-guided robots in contact with unknown environments. *IEEE Trans. Robot.* **2023**, *39*, 3705–3721. [CrossRef]
11. Zanella, R.; Palli, G.; Stramigioli, S.; Califano, F. Learning passive policies with virtual energy tanks in robotics. *IET Control Theory Appl.* **2024**, *18*, 541–550. [CrossRef]
12. Michel, Y.; Saveriano, M.; Lee, D. A Passivity-Based Approach for Variable Stiffness Control with Dynamical Systems. *arXiv* **2023**, arXiv:2307.09571. [CrossRef]
13. Ferraguti, F.; Talignani Landi, C.; Sabattini, L.; Bonfè, M.; Fantuzzi, C.; Secchi, C. A variable admittance control strategy for stable physical human–robot interaction. *Int. J. Robot. Res.* **2019**, *38*, 747–765. [CrossRef]
14. Ferraguti, F.; Preda, N.; Manurung, A.; Bonfè, M.; Lambercy, O.; Gassert, R.; Muradore, R.; Fiorini, P.; Secchi, C. An Energy Tank-Based Interactive Control Architecture for Autonomous and Teleoperated Robotic Surgery. *IEEE Trans. Robot.* **2015**, *31*, 1073–1088. [CrossRef]
15. Dietrich, A.; Wu, X.; Bussmann, K.; Ott, C.; Albu-Schäffer, A.; Stramigioli, S. Passive Hierarchical Impedance Control via Energy Tanks. *IEEE Robot. Autom. Lett.* **2017**, *2*, 522–529. [CrossRef]
16. Li, Z.; Huang, H.; Song, X.; Xu, W.; Li, B. A fuzzy adaptive admittance controller for force tracking in an uncertain contact environment. *IET Control Theory Appl.* **2021**, *15*, 2158–2170. [CrossRef]